

Spin-wave susceptibility properties of graphene-phosphorene van der Waals heterolayer: The consequence of response functions on field effect transmission

Sushant Kumar Behera and Pritam Deb*

Advanced Functional Material Laboratory (AFML), Department of Physics, Tezpur University (Central University), Tezpur-784028, India.

*Corresponding author

Email address: pdeb@tezu.ernet.in (Pritam Deb)

Abstract:

We study the spin-wave susceptibility behaviour tuned via electronic structure in chosen two dimensional (2D) graphene-phosphorene (Grp-P) van der Waals (vdWs) heterostructure model combining renormalization group approach and density functional theory simulations. First, we apply Aharonov-Bohm-Coulomb-Dirac (ABCD) formulated field-theoretic renormalization group approach for the model interacting Fermi system with nearest-neighbour hopping amplitudes. Next, the renormalization group is further extended for spin wave dependent susceptibility calculations. The analytical findings are corroborated with *ab initio* electronic structure calculations of the chosen heterostructure system in local spin density approximation (LSDA) framework. We notice a Giant Stark Effect from the calculations in the Grp-P heterolayers, where a phase transition from insulator to metal occurs in the semiconducting transport channels at low bias voltage. Lastly, a dual-gate field-effect transistor is strategically proposed having on-off ratio of 10^2 based on the electric field effect transmission.

Keywords: Two-dimensional Fermi system, Renormalization group theory, Vertex response function, Spin wave susceptibility, Dual-gate field-effect transistor

I. INTRODUCTION

Atomically thin two dimensional (2D) materials, like h-BN, graphene and its family, TMDCs, black phosphorous, etc. cover interesting field of research because of their rich mechanical [1-3], electronic [4-5], optical [6-7] and electrochemical assets with an extensive variety of promising applications [8-10]. In recent times, multilayer van der Waals (vdWs) heterostructures, chemically different 2D structures, have attracted the primary research attention unlike monolayer pristine systems, like Grp/h-BN [11], Grp/TMDC [12], h-BN/TMDC [13], Grp/Silicene [14] and TMDC/TMDC [15]. While, many 2D materials (e.g. graphene and MoS₂) have efficient carrier mobilities (i.e. high on/off ratio) [16, 17], restricts their nano-dimension heterolayer device applications. In this case, strong transport is essential to inoculate the perturbations present at defected edge sites. As a result, the transport behaviour can be modulated

via electric field or gate voltage for the desired field-effect transmission. These layered 2D vdW heterostructures possess superior efficiency for carrier inoculation via barrier height modulation [18]. In this regard, phosphorene (P), newly raised elemental puckered honeycomb 2D material, possesses fascinating electronic and optical properties, such as finite direct band gap (~ 1.5 eV) and high mobility (10^3 cm²V⁻¹s⁻¹ at 300 K) due to its structural anisotropy [19-23]. Notably, black phosphorus based field effect transistors and high-frequency nano-electromechanical resonators have been validated in recent past. Moreover, phosphorene shows a giant phononic anisotropy, which is squarely reverse compared to its electronic counterpart, supporting the asymmetrical transport of electronic/holes and phonons in heterostructure form with graphene [24].

To analyze prototypic 2D model for the electronic degrees of freedom, Hubbard model is promising in the 2D planes [25]. In particular, 2D Hubbard model of weakly interacting systems are suitable candidate with attracting phenomena tuned by their carrier density and related model parameters [26, 27]. In such systems, weak interaction reveals antiferromagnetic ground state near to half filling and symmetric s-wave phase away from half filling region. Besides, conventional perturbation theory breaks down at a certain region close to the half filling region, where challenging and frequent infrared deviations raise as a concern of weakly interacting Fermion system [28, 29] and van Hove singularities [30] along with the Aharonov-Bohm potential field in 2D graphene system [31-33]. Theoretical model for 2D weakly interacting Fermi systems having challenging singularities near weakly interacting region is still lacking in the current numerical prospects for vdW heterostructures. In this regard, Renormalization Group (RG) theory is presently the most promising and well-ordered technique for 2D Fermi systems bearing challenging singularities near weakly interacting region [34, 35]. Besides the conventional perturbation theory and RG theory, few other effective reported approaches can be implemented successfully to vdW heterostructure systems [36-38].

In the present manuscript, we implement RG theory to the 2D Hubbard model of Grp-P heterostructure considering nearest neighbor hopping amplitudes of dense electron distribution profile close to half filling region [39]. Here, we particularly calculate the trend of collective two particle couplings in single loop stage, completely ignoring the inappropriate energy and linear momentum dependency, but considering vital tangential momentum dependency being a dynamic parameter. Besides, we extend the RG theory to obtain the susceptibility values to analyze the physical response of uncertainties gestured by diverging couplings in weakly interacting vdW heterostructure. Charge-density and spin-density susceptibilities and singlet function based susceptibilities have been considered during numerical calculations at various pairing symmetries.

In this aspect, spin-density phase diagram has been presented near half filling region of this 2D Hubbard model. The obtained results show the critical energy scale behavior away from the half-filled regime where the nesting is perfect. Moreover, the analytical results have been corroborated with the first principle based density functional calculations using local spin density approximation.

We use the field-theoretic approach to frame the RG formulation for the 2D Fermi systems. Moreover, we follow plane wave basis set based *ab initio* density functional theory (DFT) simulations to carry out all DFT calculations to correlate both the analytical and simulation results. The Hamiltonian with the order of second quantization [40] unfolding the massless 2D Dirac fermions is cited below, as

$$H_{SQ} = \int d\nu \xi^\dagger(\nu) \{v_F [-i\hbar\nabla + eA(\nu)] \cdot \sigma - e\gamma(\nu)\} \xi(\nu) \quad (1)$$

where ‘e’ and ‘ σ ’ are the electron charge and spin projection, respectively. The Coulomb field potential originated due to the net charge of ‘Ze’ positioned at the origin is $\gamma(\nu) = \frac{Ze}{4\pi\epsilon_0\nu}$, similarly

the Aharonov-Bohm field solenoid aligned at the same point provides $A(\nu) = \frac{\Phi}{2\pi} \left(-\frac{y}{\nu^2}, \frac{x}{\nu^2}\right)$ with a total magnetic flux of Φ . This establishes the Aharonov-Bohm-Coulomb-Dirac (ABCD) field problem in the present chosen 2D system [41-45]. The corresponding coupling presents scattering amplitude located at potential center and corresponding energy dependency is to be obtained using RG equations. QUANTUM Espresso codes [46] based on Perdew-Burke-Ernzerhof (PBE) with generalized gradient approximation (GGA) is used in our DFT calculations [47] in the framework of local spin density approximation (LSDA) i.e. all calculations are carried out taking into account the presence of electron spins with time-reversal (TR) symmetry breaking along z-axis. Supercells having larger than 20 Å lattices are considered for first principle calculations to avoid periodic images. Brillouin zone integration has been performed with a $3 \times 3 \times 1$ k points grid sampling at an energy cutoff of 60 Ry based on the Monkhorst and Pack scheme [48]. Densities of states have been obtained on a k-point sampling of $9 \times 9 \times 1$ with smearing effect at 540 Ry as charge density cut-off energy. For band structure calculations, Γ -M-K- Γ symmetry path has been followed with same parameters as self-consistency calculations.

The flow of the vertex function (Γ) and the susceptibility (χ) values have been calculated numerically using RG theory for several choices of the bare interaction, termed as the Aharonov-Bohm field potential ($U > 0$), the next nearest neighbor hopping amplitude ($t' < 0$) and the chemical

potential (μ), where t' and μ have been fixed so that the Fermi surface and particle density are approaching to ε_k and half filling (i.e. $n \approx 1$), respectively. Momentum dependent flow of the vertex functions are obtained for the three considered systems at small length scale. It is observed that the flow of the vertex function achieves a density value ($n=0.992$), i.e. close to half filling region at $t'=0$ and $\mu=-0.005$ (plotted in Fig. 1(a)). Here, the singlet part of the vertex function is taken at specified values of momenta on the Fermi surface including the values of momenta where strong renormalization of Γ occurs. Most probably, the singlet vertex function possesses its leading values supporting umklapp scattering along the diagonal direction of the k-space Brillouin zone. It is observed from the RG theory calculation that the densities decrease away from half filling (i.e. $n=1$) region in a step-like manner and the calculations come into a region where s-wave symmetry dominates with pairing correlations at necessarily low scale energy levels indicating quantum confinement (i.e. nanostructuring) in the heterostructure system.

Two types of antiferromagnetic spin-wave (incommensurate and commensurate) susceptibilities have been obtained from the numerical calculations to validate the physical instability associated with the diverging vertex function as a consequence of response functions [49-52]. It is observed that the incommensurate spin susceptibilities can be neglected compared to their respective commensurate counterparts (shown in Fig. 1(b)) due to the incommensurability parameter ($\delta \rightarrow 0$) nearing to half-filling ($\mu \rightarrow 0$). Moreover, the ratios between the two susceptibility values of monolayer system in case of weakly interacting s-wave region are in the same scale, whereas the ratios of free susceptibility is much reduced indicating the validity of response functions for 2D weakly coupled Fermi systems. Moreover, the ratio in case of hetero bilayer is much greater compared to its monolayer system. Thus, antiferromagnetic wave vector based spin-wave susceptibility dominates over coupled susceptibilities at low scale energy level (i.e. ground state), confirming the existence of antiferromagnetic ground state with rotational spin invariance.

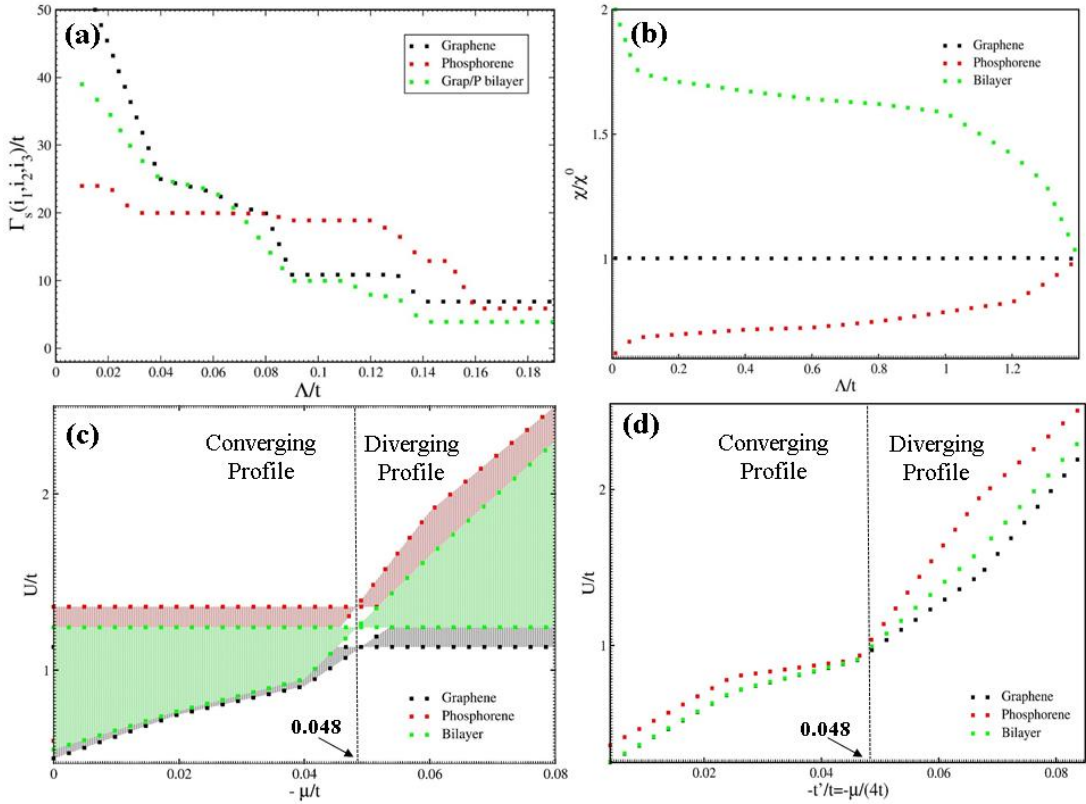


Figure 1: (a) Flow of the singlet vertex function, Γ , as a function of Λ for several selections of momenta values, k_{F1} , k_{F2} and k_{F3} . (b) The flow of the ratio of weakly interacting and free susceptibility values depending on Λ values for the three systems.

We show the phase diagram of μ and U at half filling measured by the prevailing uncertainty from the flow equation (shown in Fig. 1 (c)). The leading uncertainty region in case of commensurate spin-wave density is detached from the s-wave coupling region via a narrow strip where incommensurate spin-wave density fluctuations show dominant effect with $q=(\pi, \pi-\delta)$. For small value of U , the region surrounding half filling is exponentially small, where uncertainties in spin-wave density play a dominant effect. The (t', U) , in plane, phase diagram is shown in Fig. 1 (d) with $\mu=4t'$ and $\mu<0$ (below half-filling). It is observed that the chemical potential is fixed at the van Hove singularity [53] irrespective of the value of spin-wave density, which is decreasing away from half filling region with growing value of $|t'|$ at 0.048, one critical point in the flow equation.

The behavioral trend of critical energy scale, Λ_c , depending on the function at $t'<0$ where, $\mu=0$ and $U=t$ is plotted in Fig. 2 (a). The shrinkage in the value of Λ_c with growing trend of μ confirms that the E_F residues on the van Hove singularity within the weakly interacting regime having only Fermi surface nesting dominance. Momentum variables of the vertex function have been projected upon the Fermi surfaces at specific points, where the strong renormalization of the

vertex function occurs. Here, total 8 fixed points considered which satisfied the normalization process. Besides, additional 8 points have been considered in a more refined projection scheme upon the van Hove surface to check the collective effect. As a result, sum total 16 points (8 for Fermi surface and 8 for van Hove surface) have been taken during the flow equation. These refinements, in the response function of the spin-wave density scheme, enhance the numerical calculation efficiency significantly expressing a reasonable reduction in critical energy scale, without altering the vertex function and susceptibility values, qualitatively. The variation trend on the critical scale, Λ_c , as a function of the inverse number of discretization points, N_0 , upon the Fermi surface at fixed choice of model parameters is shown in Fig. 2(b). It is noticed that the critical energy scale is varying in a discrete manner with 8 discretization points, and resumes stability for next 8 points with right order of magnitude indicating the controlled trend of flow equation for weakly interacting systems.

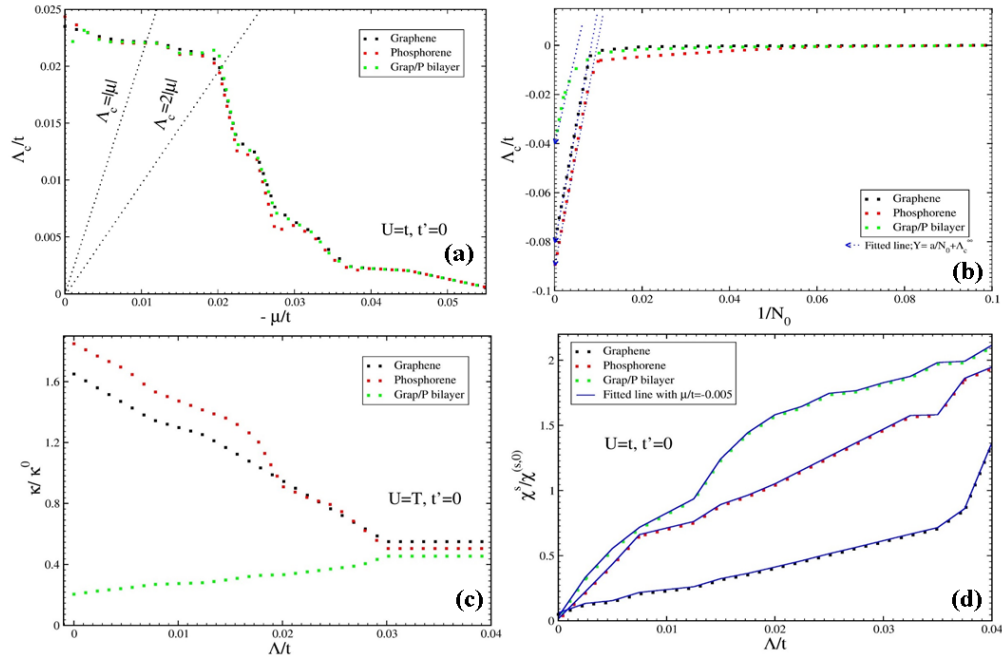


Figure 2: The critical energy scale, Λ_c , as a function of (a) μ at $U=t$ and $t'=0$. (b) number of discretization points, N_0 , upon Fermi surface at $U=t$, $t'=0$ and $\mu = -0.005$. The flow of (c) compressibility and (d) homogeneous spin susceptibility as a function of Λ .

The values of compressibility and homogeneous spin susceptibility have been calculated depending on the energy scale (shown in Fig. 2(c) and (d)), respectively for the three systems. These two parameters can be realized directly from the forward scattering of vertex function via using the Landau equations of Fermi-liquid theory [54]. The free compressibility, k^0 , and spin-wave susceptibility, $\chi^{(s,0)}$, are refined ignoring infrared cut-off values as per the Fermi-Liquid theory. As a result, the flow equations of the vertex response function is entirely because of the

flow of the Landau functions at the initial stage of the normal random phase approximation of the Hubbard model at critical energy scale value, $\Lambda=\Lambda_0$. The compressibility is inhibited at low scale energy levels near to half filling region, which is expected for systems having a finite bandgap near to ‘ μ ’, with dominant uncertainty in spin-wave density. Besides, the values of the compressibility diverge with respect to the reduction in homogeneous spin-wave susceptibility values away from half filling region, where s-wave uncertainties play major role acting indicating a finite spin-wave bandgap opening trend in any singlet or triplet spin-wave 2D Fermi systems [55]. It is found that the spin-wave susceptibility flows from zero to negative values which implies that our single loop calculation fails, when it reaches strongly interacting regime. This trend is validated only in weakly interacting region applied for 2D Fermi system. Thus, one diverging compressibility is found mentioning a strong tendency toward phase transition and separation. As a result, the increase of k sets is very close to the uncertainty, where the renormalized interactions achieve large value that the single loop findings are not further validated. The stability is prominent at higher energy scales (i.e. $0.04 \leq \frac{\Lambda}{t} \geq 0.03$) from the plot in Fig. 2((c) and (d)). Moreover, we have shown the trend of free susceptibilities (χ^0) at specific choice of t and μ values (shown in appendix Fig. 7) which is strongly supporting the trend of homogeneous spin susceptibility.

The optimized structures of the heterolayers are obtained via geometry optimization following Broyden-Fletcher-Goldfarb-Shanno (BFGS) algorithm [56]. The stable geometry of respective monolayer unit cells are shown in Fig. 3((a) and (b)) with their respective k-space first brillouin zone view in Fig. 3 (d) and (e), respectively, whereas the Grp-P hetero bilayer is shown in Fig. 3 ((c), (g) and (h)) with its k-space first brillouin zone view in Fig. 3 (f). Their optimized geometry and corresponding interlayer distances (shown in appendix Fig. 8 and Supplementary Table S1) are determined by employing the atomic structure optimization with the vdW corrections [57].

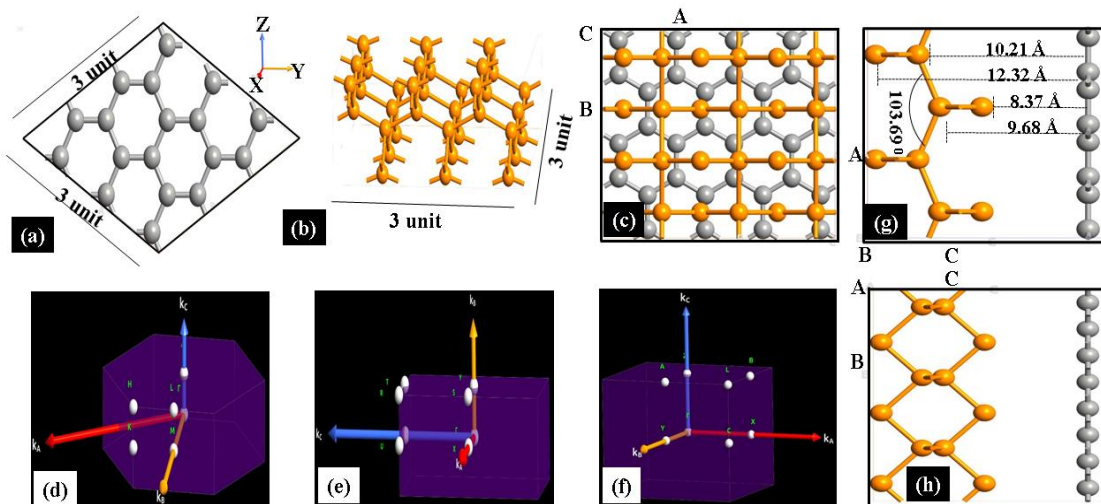


Figure 3: Atomic Configuration after optimization with David diagonalization [58]. It is 3x3x1 configuration of (a) Graphene and (b) Phosphorene unit cells in horizontal view. Bird eye view of Grp-P heterostructure in (c) XY, (g) ZX and (h) ZY plane. The first Brillouin zone (BZ) for (d) graphene, (e) phosphorene and (f) Grp-P bilayer heterostructure are shown here for reference.

The density of states (DOS) patterns for the systems have been plotted to check the number of states (shown in Fig. 4 (a)-(b)) and respective band structures (shown in Fig. 5) at various chemical potential values. Moreover, the electron density profile (shown in appendix Fig. 9) has been plotted to confirm the stable model of the 2D vdW hetero bilayer formation, irrespective of structural instabilities mentioned in the above discussed numerical session. The states are slightly flat near Fermi (E_F) region in case of Grp-P bilayer structure indicating a finite gap of 0.13 eV. It has been observed that the states present in valence band are almost twice than the states in the conduction band, indicating the effect of double number of spinors in case of LSDA approach. To realize the presence and contribution of atomic orbitals, the calculated DOS has been projected to the k-space to get projected atomic wave function value in projected density of states (PDOS) format. Here, we have resolved the case for carbon and phosphorous atoms to show the PDOS (shown in appendix Fig. 10 ((a), (b) and (c))). This orbital wave function value got replicated in case of bilayer due to twice the number of spinors (i.e. one spinor for up spin and one for down spin), like the case of DOS. This PDOS pattern reflects significant orbital splitting which is supported by the respective band structure (shown in Fig. 5).

To understand the origin of the magnetic moment in the bilayer to correlate with the susceptibility results, we have implemented the LSDA case and plot the states shown in Fig. 4((c)-(e)). It is observed that the monolayer and bilayer systems obtain small positive value of moments per atom (shown in Table S2), but subsequently the value tends to zero with minute positive value of moment indicating active antiferromagnetic ground state. The small positive value of moment can be attributed towards the spin canting effect [59, 60] in the system. An interplanar spacing is maintained between graphene and phosphorene monolayers to complete the simulation and the findings are corroborated with the analytical results for future electronic device applications.

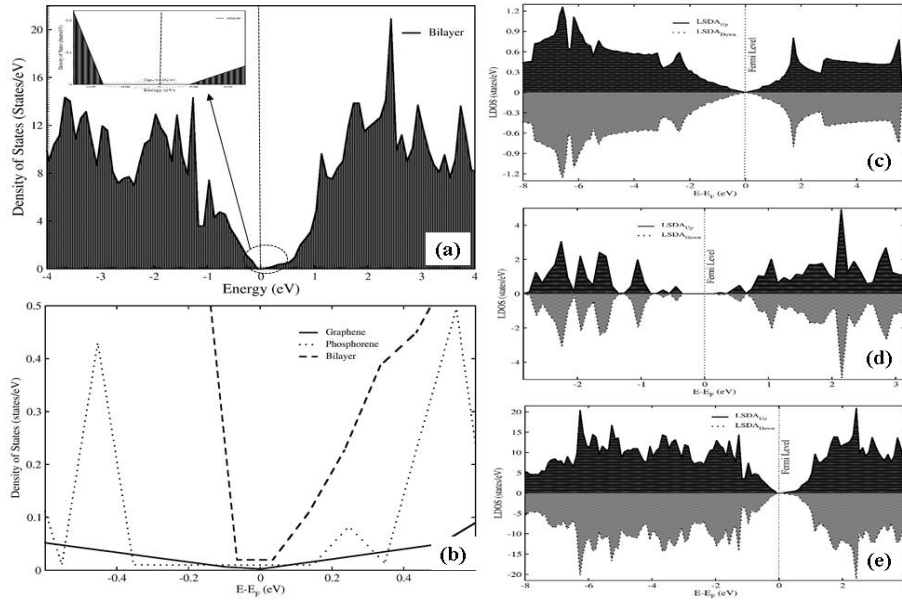


Figure 4: Density of States (DOS) of (a) Grp-P hetero bilayer with inset of the zoomed version of gap presentation. (b) TDOS of three systems, i.e. graphene, phosphorene and bilayer. Local spin density approximation (LSDA) based DOS calculation of (c) graphene, (d) phosphorene and (e) Grp-P bilayer. Both up and down states are calculated with activated spin component. Fermi level ($E_F=0$ eV) is given by the black dotted line.

It is clear from the band structure plotting that the bands related to the hetero bilayer system are away from the Fermi energy level (shown in Fig. 5) with a variation in chemical potential (μ) from -0.005 to -0.5 maintaining the variation within 10^2 order. As a result, the graphene layer blocks the stable heterostructure formation considering relevant structural instabilities within the structure along with relevant low scale energy levels of the phosphorene sheet, but unlocks a trivial finite direct bandgap (0.13 eV) at the Dirac, $\Gamma(0, 0)$, point without spin-orbit coupling. Moreover, we have altered the μ value from -0.005 to -0.5 with an increment of 10^1 order to understand the effect on bandgap in tuning the density profile. The bandgap is tuned in the range of ~ 14 meV. So, it can be preferred to use the monolayer of graphene sheet and the results can be subsequently applied in the case of the several sandwich layers [3] to develop heterolayer systems. Besides, it is noticed that there is not much qualitative changes apart from the gap-opening in hetero bilayer case. This results strongly encourages significant antiferromagnetic ordering at ground state with rotational spin invariance in such 2D weakly interacting Fermi systems, which is in direct alignment with numerical results discussed above as a consequence of response functions. Moreover, this study can be systematically proceeded to investigate the weak-coupling expansion coefficients including higher orders in a loop expansion in terms of specified Feynman diagrams and Kosterlitz-Thouless phase transition at a low scale energy levels in future.

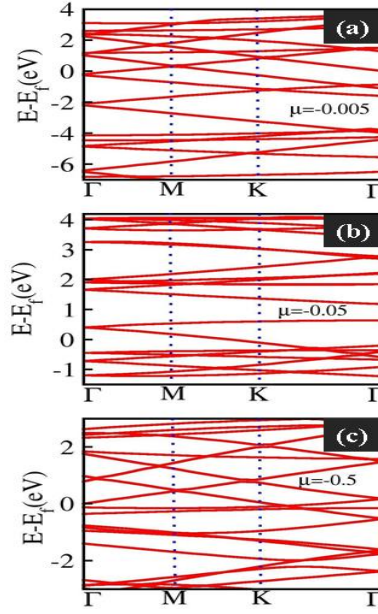


Figure 5: Electronic band structure of Grp-P hetero bilayer structure at symmetric k-points with a variation in chemical potential (μ) value of (a) -0.005, (b) -0.05 and (c) -0.5.

We demonstrate the hetero bilayer dual-gate-field effect transistors (DG-FETs) can have high *on-off* ratio considering Grp-P bilayer as a model system (shown in Fig. 6(a)). The mechanism of Giant Stark Effect is implemented here to design the vdW heterolayer-based dual-gate FET, where unsaturated Grp-P bilayers are acting as electrodes [61, 62] at room temperature. In this aspect, direct device application through Aharonov-Bohm field potential is unrealistic in pristine monolayer form, until and unless corroborated with heterolayer system using *ab initio* pseudopotential method. It is not a secret that there is no experimental evidence in condensed matter physics for the realization of the model solenoid that could produce the Aharonov-Bohm field in monolayer system. Besides, the only possibility to realize such field can be proceeded via perturbed system using a pseudopotential method (i.e. DFT simulation), which is similar to the Aharonov-Bohm vector field potential [63]. Here, saturated Grp-P bilayers serve as electrode-cum-tunneling barriers in the crucial part of the model device having dual (i.e. top and bottom) gates to generate a transverse electric field. It is evident that all phosphorus based FETs can neglect the metal to semiconductor contact at the interface for this transport behaviour. The transmission band spectrum of the model dual-gate FET at 0 V/nm and 5 V/nm, electric fields free from source to drain voltage is shown in Fig. 6 (b) at 300 K. The semiconducting characteristic of the saturated Grp-P heterolayer blocks the transmission process near the Fermi level at 0 V/nm electric field, originating a finite transmission gap of 1.12 eV, as a result, there is no transmission states near Fermi level. This absence of states indicates the *off* state of the device. Similarly, a transmission peak emerges near the Fermi level with a wide range of varying dispersion (i.e. -0.07 to +0.08 eV), at 5 V/nm electric field value, which is an unusual Van Hove-like singularity in 2D materials. This

supports the *on* state of the designed dual-gate FET, which is stable at 300 K. The transmission eigenchannels at E and at the $\Gamma(0, 0)$ point of the reciprocal k-space, presented in Fig. 6 (c) & (d), intensely illustrate the *off* and the *on* state of the designed FET controlled by a dual-gate induced electric field, respectively.

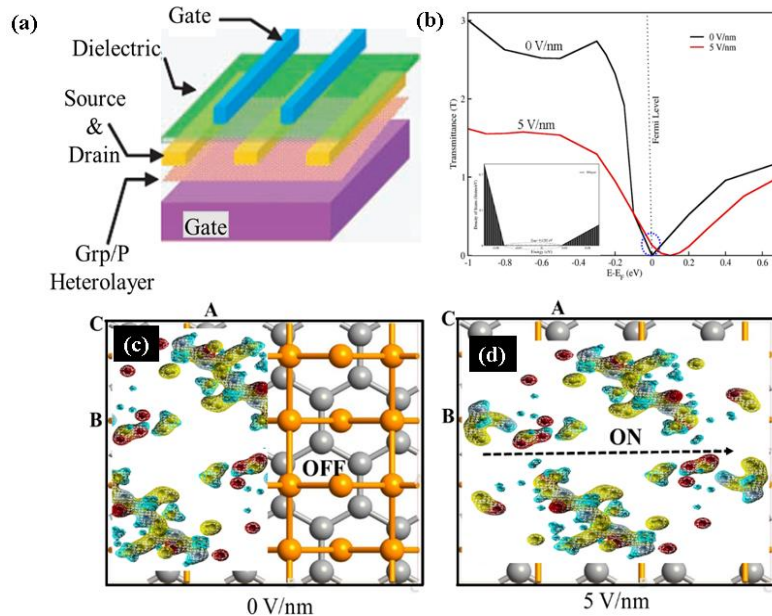


Figure 6: (a) Illustration of the chosen dual-gate FET formed from Grp-P hetero bilayer. (b) Transmission bands at 0 V/nm (black line) and 5 V/nm (red line). Inset: the DOS of the hetero bilayer system (in the scattering region) at 0 V/nm at 300 K. Transmission eigenstates at E_F and $\Gamma(0, 0)$ point in the reciprocal k space at (c) *off* state (0 V/nm) and (d) *on* state (5 V/nm) at room temperature.

The ratio of the on-off state is found to be 10^2 which indicates the persistent of quantum confinement effect due to nanostructuring in the vdW heterostructure. The value of this model hetero bilayer based dual-gate FET is 3 order higher than pristine phosphorene FETs [64] and 1 order higher compared to graphene-MoS₂ based FETs at nanoscale [65, 64]. The calculated density of states of the scattering region at 5 V/nm as an external electric field is inset in Fig. 6(b). The calculated DOS pattern indicates a distinct finite peak near the Fermi level, implying a strong correlation between the transmission channels and the density of states. The physics behind such strong correlation shows that the transport phenomena is mainly dominated by resonant tunneling through interface states [referring to Fig. 6 (c) and (d)].

In conclusion, Grp-P based vdW heterostructure system has been investigated from a field-theory perspective implementing analytical and *ab initio* electronic structure calculations. This formulation can be used to identify structural uncertainties in 2D weakly interacting Fermi systems. In this systems, critical energy can be scaled at singular points where vertex functions

and susceptibilities diverge and becomes finite particularly at reasonably weak coupling regime. Moreover, the instabilities are modulated via short range antiferromagnetic correlations present in the system, which is noticed from the vertex function flow and susceptibilities. This antiferromagnetic ordering is retained in the ground state of such 2D systems accompanied with rotational spin invariance. The computational LSDA based pseudopotential calculations corroborate the analytical results to present the correlation of band gap opening in the system (shown in Fig. S1). A significant transmission peak appears near Fermi level having large dispersion (-0.07 to +0.08 eV) with an applied electric field value of 5 V/nm, which is an unusual singularity of Van Hove kind in 2D heterostructure. This finding supports room temperature stability and on-state modelling of the system as dual-gate bilayer-FET device via pseudopotential method.

S.K.B. acknowledges Department of Science & Technology (DST), Government of India for providing financial support in terms of INSPIRE Fellowship. The authors would like to thank Tezpur University for providing High Performing Cluster Computing (HPCC) facility.

Appendix

In Fig. 7, we have shown the Free Susceptibilities variation with respect to flow equation of the system. Strain vs Interplanar distance to fix the minimum energy based configuration of the graphene/phosphorene heterolayer is shown in Fig. 8. Electron density of the 2D bilayer structure is shown in Fig. 9 to fix the electron charge density. Partial density of states of the same bilayer is plotted in Fig. 10 to find out the orbital contribution.

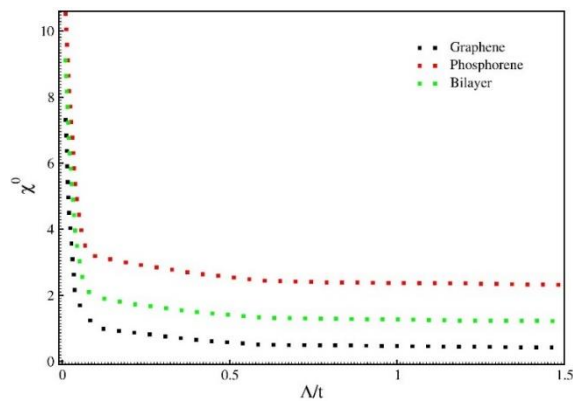


Figure 7: Free susceptibilities of graphene monolayer, phosphorene monolayer and graphene-phosphorene bilayer.

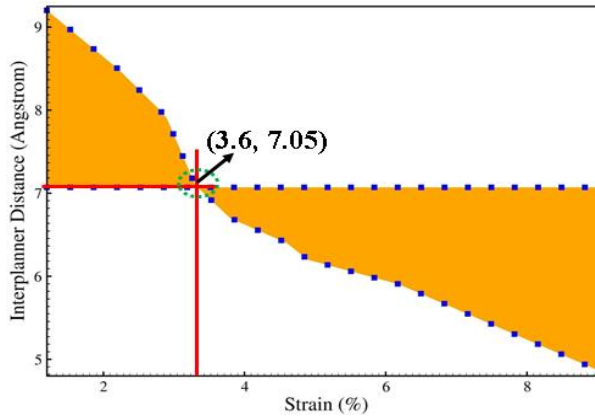


Figure 8: (a) Strain vs Interplanar distance to fix the minimum energy based configuration of the graphene/phosphorene heterolayer. Atomic Configuration after optimization has been followed with David diagonalization.

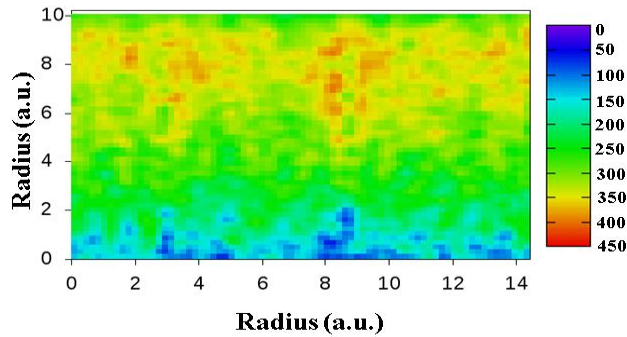


Figure 9: Electron density of the 2D graphene/phosphorene bilayer structure. The color scale is given in right hand side varying from violate to red regime. The calculation has been done in 2D scale with radius as parameter.

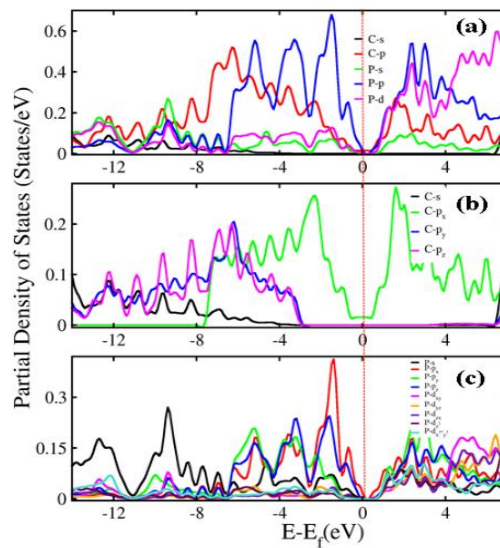


Figure 10: Partial density of states of the same bilayer with (a) local dos, (b) spectral splitting of carbon orbitals and (c) the same splitting of phosphorous. Fermi level ($E_f = 0$ eV) is given by the red dotted line.

REFERENCES

- [1] K. S. Novoselov et al., *Science* **306**, 666 (2004).
- [2] T. Georgiou et al, *Nat. Nanotechnol.* **8**, 100103 (2013).
- [3] A. K. Geim et al., *Science* **324**, 1530 (2009).
- [4] Y. Cai, G. Zhang and Y.-W. Zhang, *J. Am. Chem. Soc.* **136**, 6269 (2014).
- [5] K. Novoselov et al., *Nature* **438**, 197 (2005).
- [6] A. H. Castro Neto et al., *Rev. Mod. Phys.* **81**, 109 (2009).
- [7] X. Xu, W. Yao, D. Xiao and T. F. Heinz, *Nat. Phys.* **10**, 343 (2014).
- [8] M. I. Katsnelson, *Mater. Today* **10**, 20 (2007).
- [9] A. Pulkin and O. V. Yazyev, *Phys. Rev. B* **93**, 041419 (2016);
- [10] S. K. Behera, P. Deb and A. Ghosh, *Phys. Chem. Chem. Phys.* **18** (33), 23220 (2016).
- [11] S. K. Behera and P. Deb, *RSC Advances*, **7** (50), 31393 (2017).
- [12] S. K. Behera, P. Deb and A. Ghosh, *Chemistry Select* **2**(13), 3657 (2017).
- [13] Z. Huang, C. He, X. Qi, H. Yang, W. Liu, X. Wei, X. Peng and J. Zhong, *J. Phys. D: Appl. Phys.* **47**, 075301 (2014).
- [14] H. Wang, F. Liu, W. Fu, Z. Fang, W. Zhou and Z. Liu, *Nanoscale* **6**, 12250 (2014).
- [15] Y. Deng, Z. Luo, N. J. Conrad, H. Liu, Y. Gong, S. Najmaei, P. M. Ajayan, J. Lou, X. Xu and P. D. Ye, *ACS Nano* **8**, 8292 (2014).
- [16] F. Schwierz, *Nat. Nanotechnol.* **5**, 487 (2010).
- [17] B. Radisavljevic, A. Radenovic, J. Brivio, V. Giacometti, and A. Kis, *Nat. Nanotechnol.* **6**, 147 (2011).
- [18] C. Yongqing, G. Zhang and Y. -W. Zhang, *J. Phys. Chem. C* **119**, 13929 (2015).
- [19] A. N. Rudenko and M. I. Katsnelson, *Phys. Rev. B* **89**, 201408(R) (2014).
- [20] J. Yuan, S. Najmaei, Z. Zhang, J. Zhang, S. Lei, P. M. Ajayan, B. I. Yakobson and J. Lou, *ACS Nano* **9**, 555 (2015).
- [21] A. N. Rudenko et al., *Phys. Rev. Lett.* **116**, 246401 (2016).
- [22] L. Li, Y. Yu, G. Ye, Q. Ge, X. Ou, H. Wu, D. Feng, X. H. Chen and Y. Zhang, *Nat. Nanotechnol.* **9**, 372 (2014).
- [23] A. Nemilentsau et al., *Phys. Rev. Lett.* **116**, 066804 (2016).
- [24] Y. Shi et al, *Nano Lett.* **12**, 2784 (2012).

- [25] A. Montorsi, The Hubbard Model. World Scientific, Singapore (1992).
- [26] J. P. F. LeBlanc et al., Phys. Rev. X **5**, 041041 (2015).
- [27] A. Giuliani, V. Mastropietro and M. Porta: arXiv: 1602.01021.
- [28] K. G. Wilson, Rev. Mod. Phys. **47**, 773 (1975).
- [29] R. Shankar, Rev. Mod. Phys. **66**, 129 (1994).
- [30] N. E. Bickers, D. J. Scalapino and S. R. White, Phys. Rev. Lett. **62**, 961 (1989).
- [31] A. O. Slobodeniuk et al., Phys. Rev. B **82**, 075316 (2010).
- [32] A. O. Slobodeniuk et al., Phys. Rev. B **84**, 125306 (2011).
- [33] E. A. Stepanov and V. Ch. Zhukovsky, Phys. Rev. B **94**, 094101 (2016)
- [34] N. Furukawa, T. M. Rice and M. Salmhofer, Phys. Rev. Lett. **81**, 3195 (1998).
- [35] M. Salmhofer, Commun. Math. Phys. **194**, 249 (1998).
- [36] T. O. Wehling et al., Phys. Rev. Lett. **106**, 236805 (2011).
- [37] B. Sachs et al., Phys. Rev. B **84**, 195414 (2011).
- [38] M. Rösner et al., Phys. Rev. B **90**, 245105 (2014).
- [39] R. E. Groenewald et al., Phys. Rev. B **93**, 205145 (2016).
- [40] J. W. Negele and H. Orland, Quantum Many Particle Systems. *Addison-Wesley*, Reading, MA (1987).
- [41] M. O. Goerbig, Rev. Mod. Phys. **83**, 1193 (2011).
- [42] Y. Aharonov and D. Bohm, Phys. Rev. **115**, 485 (1959).
- [43] B. J. Dalton, J. Jeffers and S. M. Barnett, Annals of Physics **370**, 12 (2016).
- [44] N. H. March, W. H. Young and S. Sampanthar, The Many-Body Problem in Quantum Mechanics, Cambridge University Press, Cambridge, UK (1967).
- [45] K. E. Newman and E. K. Riedel, Phys. Rev. B **25**, 264 (1982).
- [46] P. Giannozzi et al, J Phys: Condens. Matter, **21**(39), 395502 (2009).
- [47] P. E. Blöch, Phys. Rev. B **50**, 17953 (1994).
- [48] H. J. Monkhorst and J. Pack, Phys. Rev. B **13**, 5188 (1976).
- [49] M. K. Chan et al, Nat Commun. **7**, 10819 (2016).
- [50] T. E. Mason et al, Phys. Rev. Lett. **68**, 1414 (1992).
- [51] S. A. Kivelson et al, Rev. Mod. Phys. **75**, 1201 (2003).
- [52] S. Higashitani, Phys. Rev. B **89**, 184505 (2014).
- [53] R. Žitko, J. Bonča and T. Pruschke, Phys. Rev. B **80**, 245112 (2009).
- [54] G. Y. Chitov and D. Sénéchal, Phys. Rev. B **57**, 1444 (1998).
- [55] V. B. Shenoy, Phys. Rev. A **88**, 033609 (2013).
- [56] J. D. Head and M. C. Zerner, Chem. Phys. Lett. **122**, 264 (1985).

- [57] R. W. Williams and D. Malhotra, Chem. Phys. **327**(1), 54 (2006).
- [58] E. R. Davidson, J. Comput. Phys. **17**, 87 (1975).
- [59] F. T. Parker, M. W. Foster, D. T. Margulies and A. E. Berkowitz, Phys. Rev. B **47**, 7885 (1993).
- [60] G. R. Blake, T. T. M. Palstra, Y. Ren, A. A. Nugroho and A. A. Menovsky, Phys. Rev. B, **65**, 174112 (2002).
- [61] Q. Wu et al, Phys. Rev. B **92**, 035436 (2015).
- [62] X. Peng, Q. Wei, and A. Copple, Phys. Rev. B **90**, 085402 (2014).
- [63] De Juan et al., Nature Physics **7**, 810 (2011).
- [64] S. P. Koenig, R. A. Doganov, H. Schmidt, A. C. Neto and B. Oezylmaz, Appl. Phys. Lett. **104**, 103106 (2014).
- [65] L. Li, Y. Yu, G. J. Ye, Q. Ge, X. Ou, H. Wu, D. Feng, X. H. Chen, and Y. Zhang, Nat. Nanotechnol. **9**, 372 (2014).

Supplementary Information

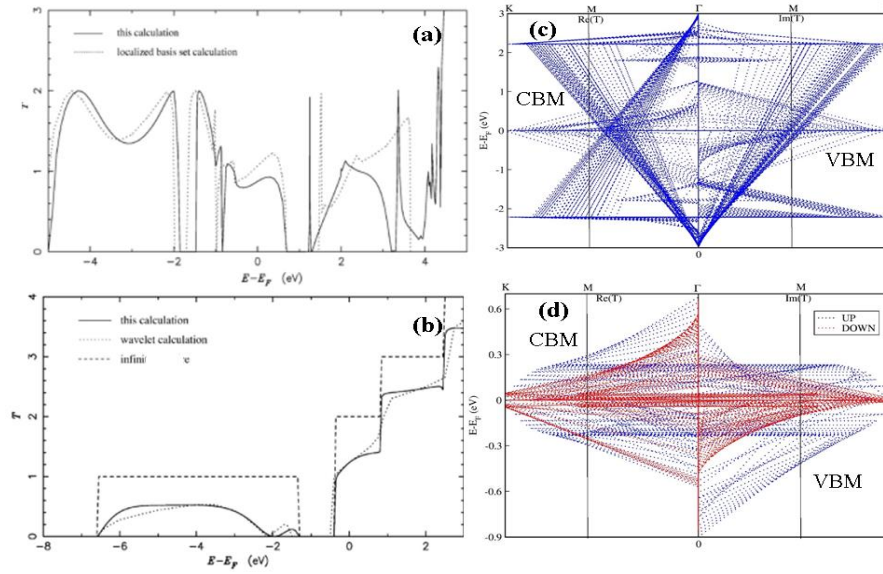


Figure S1: The transmission coefficient [1] for (a) unit cell and (b) supercell of the bilayer between two finite cross-section P electrodes. Complex band structure of the bilayer for (c) PAW and (d) the majority (spin up) and minority (spin down) states of LSDA.

Table S1: The table shows the variation configurational dimensional with strain to fix the optimized structure. David diazotization method [2] is followed to optimize the geometry with various atomic configurations. It is found that $3 \times 3 \times 1$ geometry configuration achieves minimum energy value to form stable heterolayer with the given algorithm of optimization for self-consistent field (scf) calculations.

Strain (%)	Layer Geometrical Configuration	Distance (\AA)	Optimization Energy Value (eV)
1.2	1x1x1	9.2	-13.267
2.2	2x1x1	8.5	-12.9801
2.8	2x2x1	7.6	-11.678
2.9	3x1x1	7.3	-11.2131
3.1	3x2x1	7.1	-10.0071
3.6 (scf case)	3x3x1	7.05	-9.4970
4.7	4x1x1	6.8	-12.706
8.2	9x9x1	5.2	-11.9801

Table S2: This table shows the values of the magnetic moment with respect to bandgap in bilayer at various chemical potential values. This table shows minute non-zero values of moment prevails per atom which is due to spin canting mechanism [3-5]. This non-zero values of moment signifies the antiferromagnetic nature in the ground state of the heterolayer.

Systems	Initial Moment (μ_B /atom)	Final Moment (μ_B /atom)
Graphene	0.02	0.0001
Phosphorene	0.71	0.00412
Grp/P Bilayer	0.820	0.00093

References

- [1] S. Datta, Phys. Rev. B **45** (3), 1347 (1992).
- [2] E. R. Davidson. J. Comput. Phys. 17, 87 (1975).
- [3] F. T. Parker, M. W. Foster, D. T. Margulies and A. E. Berkowitz, Phys. Rev. B **47**, 7885 (1993).
- [4] G. R. Blake, T. T. M. Palstra, Y. Ren, A. A. Nugroho and A. A. Menovsky, Phys. Rev. B, **65**, 174112 (2002).
- [5] R. Winpenny, Molecular Cluster Magnets. World Scientific, p.119. (2011): ISBN 9789814322942.
